



## Smouldering in fixed beds of oil shale grains: governing parameters and global regimes

G. Debenest , V. V. Mourzenko & J. -F. Thovert

To cite this article: G. Debenest , V. V. Mourzenko & J. -F. Thovert (2005) Smouldering in fixed beds of oil shale grains: governing parameters and global regimes, Combustion Theory and Modelling, 9:2, 301-321, DOI: [10.1080/13647830500098365](https://doi.org/10.1080/13647830500098365)

To link to this article: <http://dx.doi.org/10.1080/13647830500098365>



Published online: 20 Feb 2007.



Submit your article to this journal [↗](#)



Article views: 70



View related articles [↗](#)



Citing articles: 13 View citing articles [↗](#)

## Smouldering in fixed beds of oil shale grains: governing parameters and global regimes

G. DEBENEST, V. V. MOURZENKO and J.-F. THOVERT\*

Laboratoire de Combustion et de Détonique, CNRS

This paper examines the various regimes that may prevail in a smouldering process in a combustible porous medium, and their consequences from a physical point of view and for the formulation of a macroscopic description. A set of governing parameters are first identified, by use of a dimensional analysis. Then, their influence is illustrated by direct and detailed numerical simulations on the microscale. In particular, the lack of local thermodynamic equilibrium is demonstrated in many situations, which prevents a rash application of simple homogenized models. Finally, an application of matched microscopic and macroscopic descriptions in separate domains is presented, together with a determination of the associated effective coefficients for the latter.

### 1. Introduction

We introduced in a companion paper [1] an apparatus for the description, on the microscale, of smouldering processes in porous media, consisting of a mathematical model and the corresponding numerical simulation tool. Owing to the complexity of the problem, various simplifications had to be used (see [2] for a more detailed account). The main simplifications are to ignore the dependence of the physical properties of the constituents on temperature and to represent oxidative chemical reactions by a single-step heterogeneous reaction on the surface of the solid grains. However, the model accounts in detail for transport processes by convection and diffusion for heat and the chemical species in the gas, and by heat conduction in the solid. The local governing equations are solved explicitly, without relying on any presupposed behaviour or using any effective coefficient.

Hence, the numerical simulator can be used for at least two purposes. Direct simulations can be conducted in complex realistic situations, thus providing full and detailed knowledge of all aspects of the process and also giving access in particular to the local thermochemical conditions in the reaction sites, which control many chemical mechanisms such as the production of noxious species. Such simulations will be presented in a forthcoming paper.

On the other hand, since the model does not resort to any *a priori* hypothesis regarding the behaviours that result from the competition of many processes associated with a variety of characteristic time scales, it can be used to establish a typology of the regimes that prevail under various conditions and to assess the validity of the assumptions made in classical

---

\*Corresponding author. E-mail: [thovert@lcd.ensma.fr](mailto:thovert@lcd.ensma.fr)

macroscopic descriptions. The foremost is the hypothesis of local thermal equilibrium within each of the gas and solid phases (see e.g. [3, 4]) or even between the phases [5–9] whereby it is supposed that the temperature field can be represented by one or two locally averaged temperatures. A similar hypothesis is generally made for the oxidizer concentration in the gas. Furthermore, the macroscopic formulations involve effective coefficients for the various transport mechanisms and for exchanges between the gas and solid phases, which can be determined (when applicable) by our simulation tool.

This second type of application is the topic of the present paper, which is organized as follows. A preliminary analysis is conducted in section 2, which consists of two parts. The first one recalls some known results. The existence of two global regimes is shown, based on remarkably limited knowledge consisting of very global balance arguments and disregarding all the details of the mechanisms in the reaction zone. A basic solution in the simplest case with local thermal equilibrium is given as a reference for the discussion of subsequent results. Then, the local governing equations are formulated in a dimensionless form. Various dimensionless parameters are shown to determine the global behaviour. In particular, local thermal equilibrium or lack of it is controlled by a set of Péclet numbers.

Numerical simulations are presented in section 3, to explicitly demonstrate the influence of the main governing parameters identified in the previous section. A two-dimensional model situation is used here, because milder numerical requirements allow for a faster sweep of the parameters, but most importantly because the graphical display of the whole set of local information is easier in two dimensions. Lack of local equilibrium, which impairs the validity of classical macroscopic models, is indeed observed in many situations.

However, local equilibrium is generally recovered in quiescent regions far from the reaction zone. It is shown in section 4 how an upscaled description can then be successfully applied and matched with the local three-dimensional model in the active regions. This is of great practical interest both for the formulation of appropriate boundary conditions in the microscopic simulations and in the prospect of tackling large-scale problems.

The main observations are summarized in section 5, and elements of conclusion, including simple *a priori* criteria for the typology of global and local regimes and for the validity of simplifying assumptions, are provided.

## 2. Preliminary analysis

### 2.1 Reference solution to a simple model

We introduce here a basic solution in an extremely simple case, because it provides a guideline for the interpretation of more detailed simulation results. Most of the following is classical. Schult *et al.* [6] give a much more complete discussion, but one that is based on a set of strong assumptions, including local thermodynamic equilibrium, whose validity is not *a priori* guaranteed. In addition, the assumptions are not required for establishing the main global results. Hence, we remain here at a rather coarse level, which is sufficient for our present purpose.

Let us consider in a first step a one-dimensional situation in a very long domain. We suppose that the smouldering process has already run for an arbitrary long time, and that a steady regime has been reached. A reaction zone progresses with a velocity  $U_F$ , which defines the positive orientation of the  $x$ -axis. We denote  $\epsilon_g$  and  $\epsilon_s$  the volume fractions of the gas and solid phases, respectively,  $C_g$  and  $C_s$  their volumetric heat capacities, and  $\hat{C} = \epsilon_g C_g + \epsilon_s C_s$  the global heat capacity. The gas flows with a mean interstitial velocity  $v^*$ , which can be positive (co-flow) or negative (counter-flow).

Complex mechanisms take place in the travelling reaction zone, but we do not need to detail them at this stage. Let us simply summarize the chemical processes into the following generic

reaction, with net enthalpy  $\Delta h_C$



*A priori*, all the internal variables are functions of the position, but because of the stationarity hypothesis, the temperature and the concentrations of the chemical species tend to constant values on either side as  $x$  tends to  $\pm\infty$ . In addition, local thermal equilibrium between the gas and solid phases is necessarily satisfied in these remote regions. Hence, we may introduce the two corresponding temperatures  $T_{-\infty}$  and  $T_{+\infty}$ , the oxidizer concentrations  $c_O^{\text{in}}$  and  $c_O^{\text{out}} = c_O^{\text{in}} - \Delta c_O$  in the incoming and outgoing gas, the initial fuel content in the solid  $c_C^{\text{in}}$  and the fraction  $c_C^{\text{out}} = c_C^{\text{in}} - \Delta c_C$  left unburned after the reaction front has passed. The adiabatic temperature  $T_{\text{ad}}$  can be obtained from the ratio of the volumetric heat release to the volumetric heat capacity:

$$T_{\text{ad}} = \frac{\epsilon_s \Delta c_C \Delta h_C}{\hat{C}} \quad (2)$$

Very interesting results can be deduced from elementary global arguments. To begin with, the front velocity can be related to the gas flow rate, based on simple volumetric and stoichiometric considerations

$$U_F = \frac{\epsilon_g \Delta c_O}{\epsilon_s \Delta c_C} v^* \quad (3)$$

Then, a global energy balance can be written as

$$\hat{C} U_F (T_{-\infty} - T_{+\infty}) + \epsilon_g C_g v^* (T_{+\infty} - T_{-\infty}) = \epsilon_s \Delta c_C \Delta h_C U_F = \hat{C} U_F T_{\text{ad}} \quad (4)$$

where the first term corresponds to the rate of change of internal heat, the second one to the convective fluxes in and out of the system through the upstream and downstream boundaries, and the right-hand side is the rate of heat production from the chemical reactions. From this, we can deduce that

$$T_{+\infty} - T_{-\infty} = \frac{T_{\text{ad}}}{\Delta - 1}, \quad \text{with} \quad \Delta = \frac{\epsilon_g C_g v^*}{\hat{C} U_F} = \frac{\epsilon_s C_g}{\hat{C}} \frac{\Delta c_C}{\Delta c_O} \approx \frac{C_g \Delta c_C}{C_s \Delta c_O} \quad (5)$$

The last approximate form in the above uses the fact that  $\epsilon_g C_g \ll \epsilon_s C_s$ .

From this, we can deduce that two regimes are possible, with a hot region either on the upstream or on the downstream side, which are called the reaction leading and reaction trailing cases, respectively, by Schult *et al.* [6]. For  $\Delta > 1$ , most of the heat produced in the reaction zone is convected to the downstream side, where the temperature reaches a plateau  $T_p$  above the room temperature that prevails on the far upstream side. Conversely, for  $\Delta < 1$ , most of the produced heat is left behind the reaction zone, where the temperature increases at the value  $T_p$  above that of the far downstream region. In both cases,

$$T_p = \frac{T_{\text{ad}}}{|\Delta - 1|} \quad (6)$$

Note that the terms upstream and downstream are meant here relative to the propagation of the reaction zone. Note also that this applies both for co-flow ( $v^* > 0$ ) and counter-flow ( $v^* < 0$ ) processes. In the latter case,  $\Delta$  is negative and  $T_p$  is always smaller than  $T_{\text{ad}}$ . In the case of a co-flow process,  $T_p \leq T_{\text{ad}}$  if  $\Delta \geq 2$ , but a superadiabatic regime with  $T_p > T_{\text{ad}}$  is obtained when  $0 < \Delta < 2$ . The particular case  $\Delta = 1$  is degenerate and cannot yield a stationary regime.

Interestingly, the value of  $\Delta$  depends only weakly and indirectly on the flow rate or the heat release, through their influence on  $\Delta c_C$  and  $\Delta c_O$ . In a reasonably efficient process, these are of the order of  $c_C^{\text{in}}$  and  $c_O^{\text{in}}$ , respectively, and  $\Delta$  depends only on the heat capacities and

concentrations of the constituents. Then,  $\Delta$ ,  $T_p$  and the global regime can be tuned by acting on  $c_O^{\text{in}}$  and  $c_C^{\text{in}}$ , for instance by mixing the solid fuel with a fraction of inert solid material.

All the foregoing results are based only on global balance considerations, and therefore they are very robust. In particular, they do not rely on any hypothesis of local equilibrium, except in arbitrary far upstream and downstream regions. It is quite remarkable for instance that the existence of two regimes and equation (5) can be stated regardless of the details of the processes in the reaction zone.

In order to proceed a little farther, let us introduce two simplifying hypotheses which are classically used in simple macroscopic models (see for instance [5]). Assume that the gas and solid phases are in local thermal equilibrium, so that a description in terms of a single,  $x$ -dependent temperature  $\bar{T}$  is possible, and that the reaction zone is narrow. The heat transport equation, in a referential attached to the reaction front located at  $X_F$ , takes the form of

$$\hat{C} \frac{\partial \bar{T}}{\partial t} + (\epsilon C_g v^* - \hat{C} U_F) \frac{\partial \bar{T}}{\partial x} - \hat{\lambda} \frac{\partial^2 \bar{T}}{\partial x^2} = \delta_{X_F} S_H \quad (7)$$

where the source term  $S_H = \epsilon_s \Delta c_C U_F \Delta h_C$  is localized at the origin (i.e., the front location) by the Dirac function  $\delta_{X_F}$  and  $\hat{\lambda}$  is an effective conductivity coefficient. Note that equation (4) is simply the integral of equation (7) from  $-\infty$  to  $+\infty$ . Note also that this simple model does not take into account dispersive effects, which are discussed in Section 4 and which can be quite important depending on the flow regime. By using equation (2) and denoting  $\hat{D} = \hat{\lambda}/\hat{C}$ , this can be rewritten as

$$\frac{\partial \bar{T}}{\partial t} + (\Delta - 1) U_F \frac{\partial \bar{T}}{\partial x} - \hat{D} \frac{\partial^2 \bar{T}}{\partial x^2} = \delta_{X_F} U_F T_{\text{ad}} \quad (8)$$

Plainly, the only stationary solutions to the differential equation (8) are piecewise constant or exponential functions. Owing to the continuity of temperature and to the heat flux balance (which includes the singular source  $S_H$ ) at  $X_F$ , this yields

$$\begin{aligned} & (x \leq X_F) & (x \geq X_F) \\ \text{if } \Delta > 1: & \bar{T}(x) = T_p e^{x/\Lambda} & \bar{T}(x) = T_p \end{aligned} \quad (9a)$$

$$\text{if } \Delta < 1: \quad \bar{T}(x) = T_p \quad \bar{T}(x) = T_p e^{-x/\Lambda} \quad (9b)$$

where the plateau temperature  $T_p$  is given by equation (6) and

$$\Lambda = \frac{\hat{D}}{U_F |1 - \Delta|} \quad (10)$$

In the case of  $\Delta = 1$ , equation (8) degenerates into a diffusion equation with a point source at a fixed position, and there is no stationary regime. The solution reduces to a peak around the front location, whose height increases as the square root of time. Of course, this increase cannot go on forever and it has to break out when other mechanisms take over, such as transverse heat losses.

It may seem perplexing that no mention has been made in the above of the kinetic aspects of the smouldering process, which requires at least that a high enough temperature is reached to sustain the chemical reactions. However, this is justified *a posteriori* in the framework of this simple model by the shape of the solution (9). If a stationary regime exists (and assuming that the process could somehow be initiated, by use of any ignition device), the temperature in the reaction zone settles at  $T_p$ . It can then be checked, based on a separate thermochemical criterion, whether the process is viable or not. If  $T_p$  is large enough, the solution (9) is stable; in the opposite case the process is doomed to extinction.

However, this argument applies only because the reaction zone was supposed to be narrow and because thermodynamical equilibrium was assumed. An assessment of the validity of these

simplifications and exact predictions in the likely case when they are not applicable requires a detailed examination of the mechanisms on the local scale which is the purpose of our numerical model. Furthermore, many effective coefficients including in particular the actual amounts  $\Delta c_O$  and  $\Delta c_C$  of reactants consumed in the process have to be determined. Since the width of the reaction zone can be of the order of the characteristic microscopic length scale, i.e. a few grain sizes, the application for this purpose of a macroscopic formulation such as in the inner problems of Schult *et al.* [6] is questionable; again, the solution of a local problem is required, where the microstructure of the porous medium is taken into account.

## 2.2 Dimensionless formulation and parameters

In the framework of the mathematical model given by Debenest *et al.* [1], the system is described by their equations (3), (6) and (12), which govern the oxidizer transport, the heat transport and the evolution of the fuel content in the shale grains, respectively. In addition, their equation (10) summarizes the oxidizing reaction kinetics into two regimes, with a negligible (for  $T < T_r$ ) or diffusion-limited (for  $T \geq T_r$ ) reaction rate according to the local temperature and fuel concentration. We propose here a dimensionless formulation of these equations, in order to clearly identify the main physical parameters.

Let us first define a set dimensionless variables, denoted by primes, based on: a characteristic length scale  $\mathcal{L}$ , which is equal to or of the order of the grain diameter  $\Phi$  (e.g. the period  $6\Phi/5$  of the periodic staggered array of cylinders in the two-dimensional examples); the mean interstitial gas velocity  $v^*$ ; the oxygen diffusion coefficient  $D_O$ ; and the initial fuel and oxidizer concentrations  $c_C^{\text{in}}$  and  $c_O^{\text{in}}$ .

$$\mathbf{r} = \mathcal{L} \mathbf{r}' \quad \nabla = \frac{1}{\mathcal{L}} \nabla' \quad \mathbf{v} = v^* \mathbf{v}' \quad (11a)$$

$$c_O = c_O^{\text{in}} c'_O \quad c_C = c_C^{\text{in}} c'_C \quad (11b)$$

$$t = \frac{\mathcal{L}^2}{D_O} t' \quad T = \tilde{T}_{\text{ad}} T' \quad \text{with } \tilde{T}_{\text{ad}} = p_s \frac{\epsilon_s c_C^{\text{in}} \Delta h_c}{\hat{C}} \quad (11c)$$

The temperature scale  $\tilde{T}_{\text{ad}}$  is defined as the adiabatic temperature in equation (2) (but based on the total fuel content since the unburned fraction is not known beforehand) and takes into account that the solid phase contains a volume fraction  $p_s$  of reactive oil shale, mixed with a complement of inert material. The governing equations can then be written as:

$$\frac{\partial c'_O}{\partial t'} + Pe_O \nabla' \cdot (\mathbf{v}' c'_O) - \nabla'^2 c'_O = 0 \quad \text{in } \mathcal{P} \quad (12a)$$

$$\mathbf{n}_{\mathcal{I}} \cdot \nabla' c'_O = 0 \text{ or } c'_O = 0 \quad (\text{depending on } T - T_r) \text{ on } \mathcal{I} \quad (12b)$$

$$\frac{\partial T'_g}{\partial t'} + Pe_O \nabla' \cdot (\mathbf{v}' T'_g) - Le_g \nabla'^2 T'_g = 0 \quad \text{in } \mathcal{P} \quad (12c)$$

$$\frac{\partial T'_s}{\partial t'} - Le_s \nabla'^2 T'_s = 0 \quad \text{in } \mathcal{S} \quad (12d)$$

$$T'_g = T'_s \quad \text{on } \mathcal{I} \quad (12e)$$

$$Le_g \mathbf{n}_I \cdot \nabla' T'_g - Le_s \frac{C_s}{C_g} \mathbf{n}_I \cdot \nabla' T'_s = \frac{1}{\tilde{\Delta}} \mathbf{n}_I \cdot \nabla' c'_O \quad \text{on } \mathcal{I} \quad (12f)$$

$$\frac{dc'_C}{dt'} = \frac{c_{O,C}^{\text{in}}}{c_C^{\text{in}}} \frac{1}{V'_g} \int_{\partial V'_g} \mathbf{n}_I \cdot \nabla' c'_O ds' \quad \text{per grain } V_g \quad (12g)$$

It is apparent that six dimensionless numbers determine the behaviour of the system. Five of them describe the properties of the constituents, namely the ratios of the volumetric heat capacities  $C_s/C_g$  and of the oxidizer and fuel contents  $c_{O,C}^{\text{in}}/c_C^{\text{in}}$ , the gas Lewis number  $Le_g$  and a similar ratio  $Le_s$  for the solid thermal diffusivity

$$Le_g = \frac{D_{T,g}}{D_O}, \quad Le_s = \frac{D_{T,s}}{D_O} \quad (13)$$

and a parameter  $\tilde{\Delta}$  defined as  $\Delta$  in equation (5), except for the introduction of  $p_s$  and the use of the initial concentrations in the definition of the typical front velocity  $\tilde{U}_F$

$$\tilde{U}_F = \frac{\epsilon_g c_O^{\text{in}}}{p_s \epsilon_s c_C^{\text{in}}} v^*, \quad \tilde{\Delta} = \frac{\epsilon_g C_g v^*}{\hat{C} \tilde{U}_F} = \frac{p_s \epsilon_s C_g c_C^{\text{in}}}{\hat{C} c_O^{\text{in}}} \approx \frac{p_s C_s c_C^{\text{in}}}{C_g c_O^{\text{in}}} \quad (14)$$

The last dimensionless ratio is the Péclet number  $Pe_O$ . It is an operating parameter which quantifies the gas flow rate,

$$Pe_O = \frac{v^* \mathcal{L}}{D_O} \quad (15)$$

Interestingly, the length scale  $\mathcal{L}$  appears only in the Péclet number and in the definitions of dimensionless time and position vector in equation (11). Hence, different systems obtained by a change in scale (i.e. same materials and similar microstructure, but possibly the shale has been ground into smaller or larger grains) and operated with the same Péclet number (i.e. a different gas velocity, since  $\Phi$  is different) are described by the same dimensionless equations, whose solutions will differ only by their time scales. In particular, the same global behaviours will prevail and identical temperature fields will be obtained for identical advancements  $X'_F$  of the reaction front. It should be kept in mind, however, that this exact similitude applies only under the assumption that the physical properties of the parameters do not depend on the temperature, which is of course an approximation, and because of the diffusion limited reaction kinetics. For instance, a first order kinetically controlled reaction rate would introduce at least one additional parameter, in the form of a Damkohler number.

Equation (12f) can be written in a different and instructive form,

$$\frac{\tilde{\Delta}}{Pe_{T,g}} \mathbf{n}_I \cdot \nabla' T'_g - \frac{\epsilon_g}{\epsilon_s Pe_{F,s}} \mathbf{n}_I \cdot \nabla' T'_s = \frac{1}{Pe_O} \mathbf{n}_I \cdot \nabla' c'_O \quad \text{on } \mathcal{I} \quad (16)$$

We used in the second term the approximation  $\hat{C} \approx \epsilon_s C_s$ , which corresponds in practice to a relative error smaller than  $10^{-3}$ . This introduces two new Péclet numbers:

$$Pe_{T,g} = \frac{v^* \mathcal{L}}{D_{T,g}} \quad Pe_{F,s} = \frac{\tilde{U}_F \mathcal{L}}{D_{T,s}} \quad (17)$$

They are of course not independent of the other six parameters, since

$$Pe_{T,g} = \frac{Pe_O}{Le_g} \quad Pe_{F,s} = \frac{\epsilon_g C_g Pe_O}{\hat{C} \tilde{\Delta} Le_s} \approx \frac{\epsilon_g \lambda_g}{\epsilon_s \lambda_s} \frac{Pe_O}{\tilde{\Delta} Le_g} \quad (18)$$

In addition,  $Pe_O$  and  $Pe_{T,g}$  are nearly equivalent, since  $Le_g$  is close to one. However, they clearly point out the various time scales on which the diffusive processes are acting, and they can be used for a physical discussion.

$Pe_O$  and  $Pe_{T,g}$  are the ratios of typical diffusive times in the gas,  $\mathcal{L}^2/D_O$  or  $\mathcal{L}^2/D_{T,g}$ , to the convective time  $\mathcal{L}/v^*$ . They tell us in particular whether the transverse equalization of these fields is fast or slow compared to the gas residence time, which is an important issue when trying to give a macroscopic description of the process in terms of supposedly representative local mean values. They are also crucial for the estimation of the effective exchange coefficients which are used in these upscaled models. From a physical point of view, it can be intuitively felt that for a large  $Pe_O$  the oxidizer entering a hot reactive region can be carried by the gas over a long distance before it can reach the solid surface by transverse diffusion. This will tend to increase the length of the reaction zone, and possibly cause a significant fraction of the oxidizer to escape on the downstream side.

On the other hand,  $Pe_{F,s}$  compares the characteristic time  $\mathcal{L}^2/D_{T,s}$  for heat diffusion in the solid and the typical time  $\mathcal{L}/\tilde{U}_F$  for the reaction front progress. It tells us whether the heat produced by the chemical reaction spreads in the solid faster than the front progresses, or whether thermal disequilibrium prevails in the solid in the reaction zone. Of course, the meaning of a locally averaged solid temperature can be questioned in the latter case. It can also be felt that  $Pe_{F,s}$  determines the width of the hot region around the reaction zone and controls in particular the preheating of the solid (especially when  $\tilde{\Delta} < 1$ , since convection takes care of the preheating in the opposite case), with determinant influence on the viability of the smouldering process.

In addition to the local thermal equilibrium within each of the phases, interphase thermal equilibrium is also an important issue since it underlies the choice between single- or double-temperature macroscopic models. However, because of the much larger volumetric heat capacity of the solid, the time constant for the equalization of the phase temperatures is about the same as the characteristic time for heat diffusion in the gas in the pore space. Therefore, local equilibrium in the gas (i.e. small or moderate  $Pe_{T,g}$ ) generally implies local equilibrium in the solid (since  $Pe_{F,s}$  is generally smaller than  $Pe_{T,g}$ , see table 1) and overall local equilibrium. Hence, double-temperature macroscopic models should be applied with great caution; there might be only a narrow range between regimes where the meaning of locally averaged phase temperatures is questionable and regimes where double-temperature is of little use because overall local equilibrium is fulfilled.

### 3. Numerical simulations

Two series of calculations are presented below in order to illustrate the influence of the dimensionless numbers and the resulting typology of the regimes. We kept three quantities

Table 1. Main parameters for the two series of simulations in sections 3.1 and 3.2. The adiabatic temperatures are relative to the initial bed temperature and gas temperature.

	$\tilde{\Delta}$	$Pe_O$	$Pe_{T,g}$	$Pe_{F,s}$	$U_F/v^*$	$\tilde{T}_{ad}$ (°C)
Section 3.1	0.2175	2	2.2	0.512	$3.0 \times 10^{-4}$	607
Simulation	0.2175	5	5.5	1.025	$3.0 \times 10^{-4}$	607
	0.2175	10	11.1	2.05	$3.0 \times 10^{-4}$	607
Section 3.2	0.0645	10	11.1	6.9	$1.0 \times 10^{-3}$	180
Simulation	0.157	10	11.1	2.75	$4.0 \times 10^{-4}$	437
	0.322	10	11.1	1.38	$2.0 \times 10^{-4}$	900
	0.645	10	11.1	0.69	$1.0 \times 10^{-4}$	1800
	1.29	10	11.1	0.45	$5.0 \times 10^{-5}$	3600



constant, which only depend on the constituent physical properties, namely

$$C_s/C_g = 8500 \quad Le_g = 0.9 \quad Le_s = 1.45 \times 10^{-3} \quad (19)$$

These are typical values obtained for the materials in the reference experiment described by Debenest *et al.* [1] and Ahd *et al.* [10]. In addition, we consider that the oil shale grains are not mixed with inert solid ones, i.e.  $p_s = 1$ . Hence, we are left with two independent parameters:  $\tilde{\Delta}$ , which is a measure of the ratio  $c_O^{\text{in}}/c_C^{\text{in}}$  (see equation (14)); and  $Pe_O$ , which is an operating parameter and quantifies the gas flow rate. The two other Péclet numbers  $Pe_{T,g}$  and  $Pe_{F,s}$  result from  $Pe_O$  via equation (18).

The simulations were conducted in the 2D model medium described earlier [1], composed of a staggered array of cylinders of diameter  $\Phi$ . The geometry is spatially periodic, with a period  $\mathcal{L} = 6\Phi/5$  in the longitudinal direction and  $2\Phi$  in the transverse direction. The porosity is  $\epsilon_g = 0.353$ . This 2D setting allows for an easier graphical display of the local temperature and concentration fields than more realistic 3D media, which is precisely what we are presently interested in.

In the presentation of the results, we use the length  $X_F = \tilde{U}_F t$  (or its dimensionless counterpart  $X'_F = X_F/\mathcal{L}$ ) as a measure of the elapsed time since ignition. This corresponds to the expected position of the reaction front when both the fuel and oxidizer are exhausted. This is not guaranteed in general, albeit it turns out that it is nearly true in most cases. In any case,  $X'_F$  is a convenient dimensionless measure of time. In all the pictures that follow, the gas flows from the left to the right.

### 3.1 Influence of $Pe_O$

In this first set of simulations, the value of  $\tilde{\Delta}$  was kept constant and equal to 0.2175. This corresponds to a fuel content  $c_C^{\text{in}} = 5195 \text{ mol/m}^3$  in the shale, if the oxygen concentration correspond to standard air ( $c_O^{\text{in}} = 2.8 \text{ mol/m}^3$  at 1000 K), and it was deduced from experimental measurements of the front velocity in the reference experiment. The Péclet number  $Pe_O$  was set equal to 2, 5 or 10, which covers the experimental range of the gas flow rate (partial fluidization of the bed occurs for larger values). The main parameters are summarized in table 1, where the adiabatic temperature  $\tilde{T}_{\text{ad}}$  was obtained from equation (11c) with  $\Delta h_c = 395 \text{ kJ/mol}$ .

Consider first figure 1, which corresponds to  $Pe_O = 5$ , and provides a graphic summary of a simulation run. The medium is initially at room temperature, as is the gas blown at the inlet. In order to initiate the process, the simulations are run at first with  $T_r = 0$ , i.e. by ignoring the dependence of the oxidizing reaction rate on the temperature, and assuming that it is always limited by the oxidizer supply or by the fuel exhaustion. As time passes, the reaction front progresses and a fairly steady travelling pattern is eventually reached. The temperature field is shown in figure 1 at successive regularly spaced instants, which correspond to increasing positions  $X'_F$  of the reaction front. Since  $T_r = 0$ , both the fuel and oxidizer are indeed exhausted, and  $\tilde{U}_F$  exactly corresponds to the front propagation velocity. The reaction zone extends over about a  $2\mathcal{L}$  interval which is always centered at  $X_F$ . The last frame shows the oxidizer and fuel concentrations  $c'_O$  and  $c'_C$  in the last stage ( $X'_F = 14$ ). It confirms that the fuel and the oxidizer are exhausted on the upstream and downstream sides of the front, respectively. Only two rows of solid grains are at values of  $c'_C$  different from zero and one. Figure 2 shows the colour codes used for concentration and temperature fields for subsequent figures.

Let us now compare the results for the three values of the Péclet number  $Pe_O = 2, 5$  and 10. They are given, when  $X'_F = 14$ , as maps of the local fields in figure 3 and as longitudinal

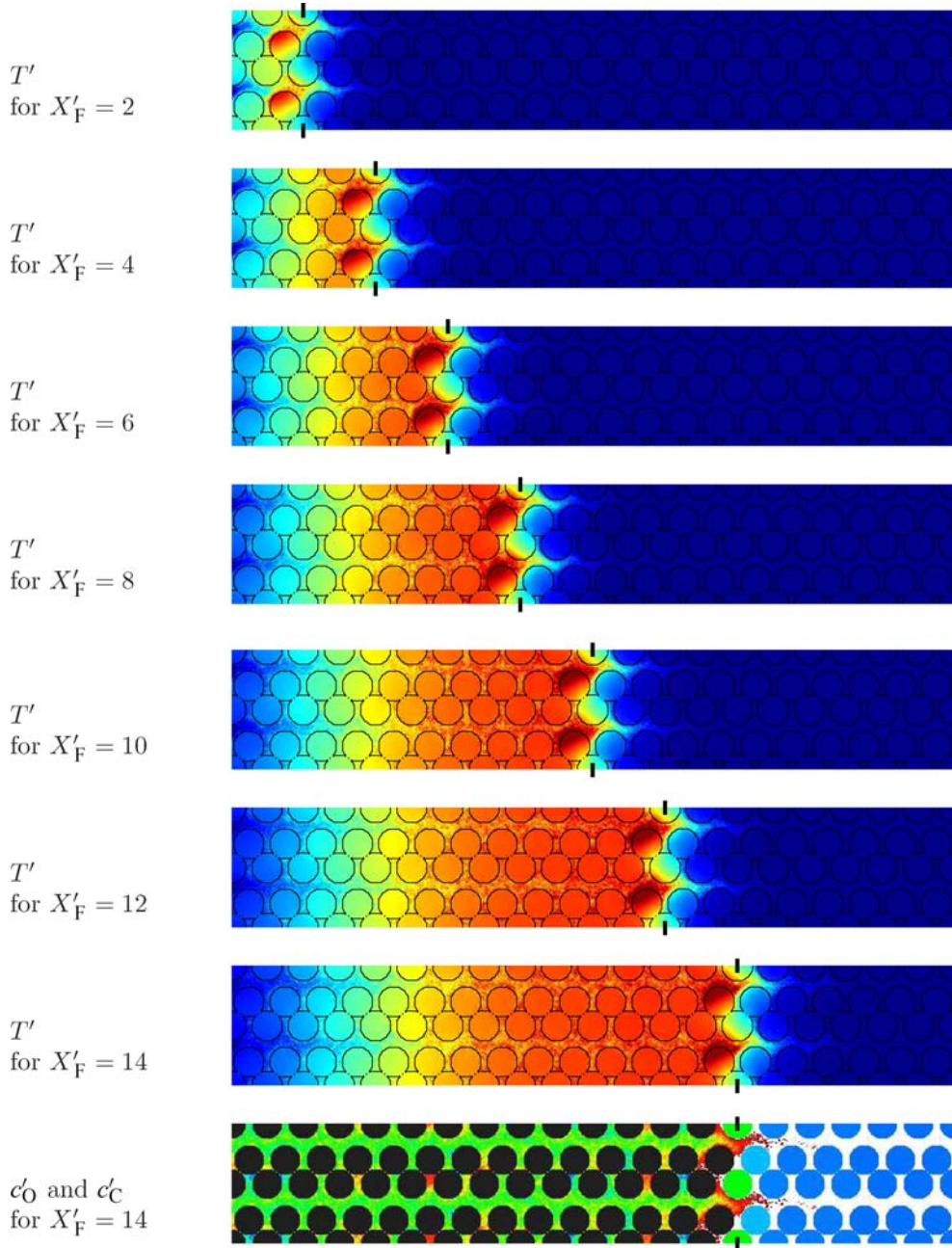


Figure 1. Temperature fields at successive times, for increasing positions  $X'_F$  of the reaction front, when  $Pe_O = 5$ ,  $\bar{\Delta} = 0.2175$  and  $T_r = 0$ . The bottom frame shows the oxidizer and fuel concentrations in the last stage. The vertical marks show the position  $X_F$ . The colour codes for  $T'$ ,  $c'_O$  and  $c'_C$  are given in figure 2.

profiles of the transversally averaged concentration  $\bar{c}'_O$  and phase temperatures,  $\bar{T}'_s$  and  $\bar{T}'_g$ , in figure 4. They obviously share some common global features. In all cases, the medium downstream of the reaction front remains at the initial temperature, while a fairly isothermal hot region develops on the upstream side, between the front and the vicinity of the inlet where cold gas is injected. This concurs with the prediction of the global arguments in section 2.1,

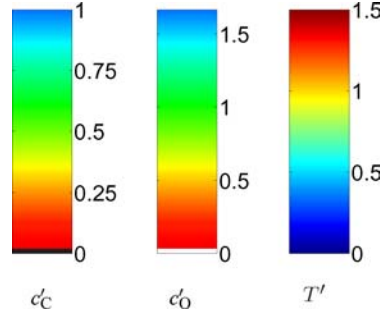


Figure 2. Colour codes used in several figures in this section for the display of concentration and temperature fields.

when  $\tilde{\Delta} < 1$ . Furthermore, the plateau temperature deduced from the profiles of  $\bar{T}'_s$  and  $\bar{T}'_g$  in figure 4, is in excellent agreement (within  $\pm 0.01$ ) with the prediction  $T'_p = 1.278$  of equation (6).

However, there are differences on a more local scale, in the transient regions around  $x' = 0$  and  $x' = X'_F$ . First, the reaction zone extension increases with  $Pe_O$ . This can be perceived qualitatively in the concentration maps in figure 3, and more quantitatively in the transversally averaged oxidizer concentration profiles in figure 4. The latter roughly obey exponential laws,  $\bar{c}'_O \propto \exp(-x'/\Lambda_O)$ , and the decay length  $\Lambda_O$  increases with the Péclet number, according to  $\Lambda_O \approx 0.082Pe_O$  ( $\pm 10\%$ ). This is natural since the oxidizer profiles result from the competition of the diffusion-limited trapping on the solid and of the convection by the gas flow.

There are also important differences in the temperature fields. Local thermal equilibrium is fairly well satisfied when  $Pe_O = 2$ , as can be seen in the map in figure 3, or from the quasi-identity of the profiles of  $\bar{T}'_g$  and  $\bar{T}'_s$  in figure 4. However, a different picture is obtained for  $Pe_O = 10$ . The profiles of the solid and gas temperatures deviate significantly in their transient parts near the inlet and downstream of the reaction front. Thermal wakes are clearly visible in figure 3,  $\bar{T}'_g < \bar{T}'_s$  in the entry region and  $\bar{T}'_g > \bar{T}'_s$  for  $x' > X'_F$ . Moreover, thermal equilibrium is not achieved within the solid phase. In the reaction zone and somewhat upstream of it, temperature strongly varies within the solid grains. Variations of  $T'$  of the order of unity can exist between two opposite sides of the same grain. This is, of course, because of the value

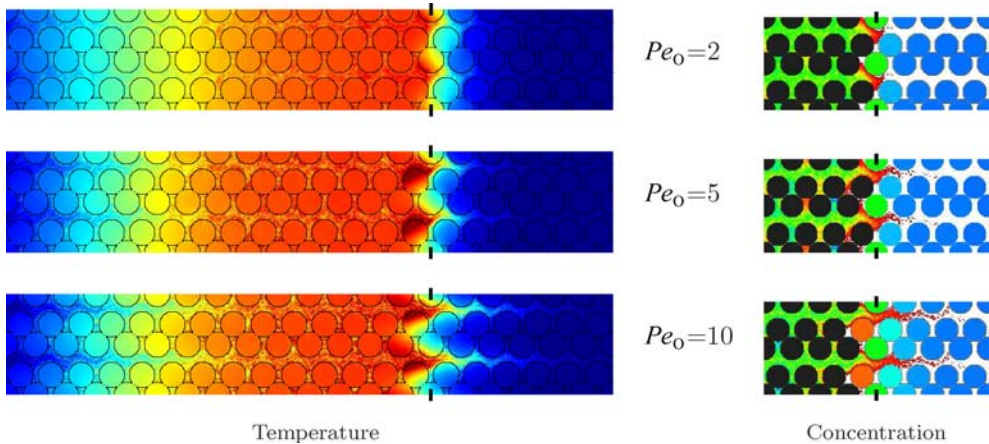


Figure 3. Temperature and concentration fields when  $X'_F = 14$ , for  $\tilde{\Delta} = 0.2175$ ,  $T_i = 0$  and  $Pe_O = 2, 5$  and  $10$ . The colour codes for  $T'$ ,  $c'_O$  and  $c'_C$  are given in figure 2. The vertical marks show the position  $X'_F$ .

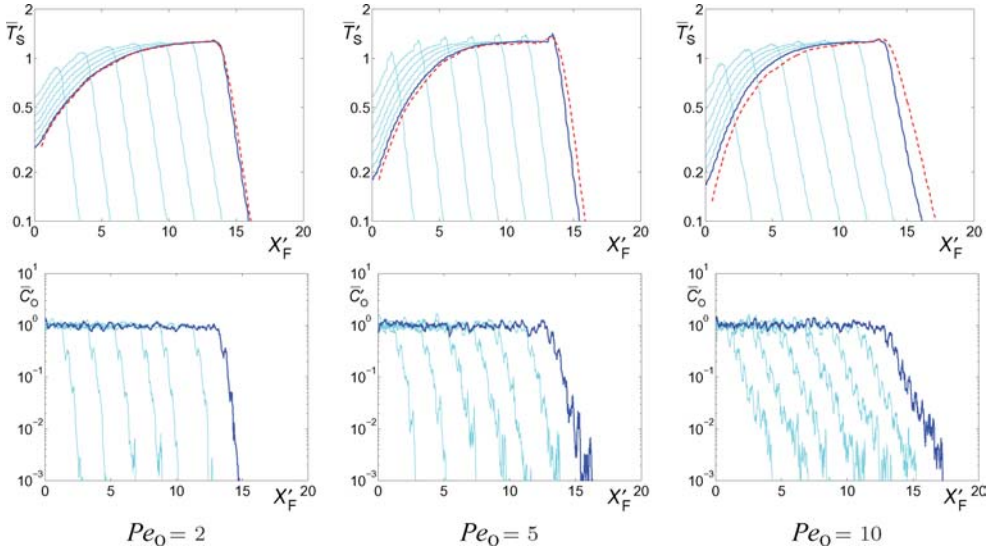


Figure 4. Profiles of the transversally averaged solid temperature  $\bar{T}'_s$  and oxygen concentration  $\bar{C}'_O$ , for  $\tilde{\Delta} = 0.2175$ ,  $T_r = 0$  and  $Pe_O = 2, 5$  and  $10$ . The profiles are given for  $X'_F = 2, 4, \dots, 12$  (light blue line) and  $14$  (dark blue line). The red broken line is the gas temperature  $\bar{T}'_g$  when  $X'_F = 14$ .

of  $Pe_{F,s} \approx 2$ , which means that it takes twice as long for heat to spread within a grain than for the front to advance by a grain diameter.

Quite naturally,  $Pe_O = 5$  yields a regime intermediate between the two former ones. The thermal wakes in the gas and the deviation from equilibrium within the solid are weaker than for  $Pe_O = 10$ , but both still exist.

It should be noted that whereas the transversally averaged temperature profiles in figure 4 reveal a possible lack of interphase equilibrium, they do not provide any information regarding intraphase disequilibrium. There is no qualitative differences between the profiles of  $\bar{T}'_s$  for the various Péclet numbers, nor any indication that  $T'$  can be locally much larger than  $T'_p$ .

The simulations described so far with  $T_r = 0$  were resumed starting from the situation reached at  $X'_F = 14$ , with  $T_r = 600$  K. This value results from the measurements of Nabih *et al.* [11] for oil shales from the same region as those considered in the reference experiment, which showed that the oxidative reactions are initiated at about 500 K and that all the carbon is consumed at about 750 K. The calculations were run until  $X'_F = 22$  (for  $Pe_O = 2$ ) or 28 (for  $Pe_O = 5$  and  $10$ ). The corresponding results are shown in figures 5 and 6.

It can be observed that the introduction of the threshold temperature  $T_r$  in the reaction kinetic law has no significant influence on the global behaviours. In the case of  $Pe_O = 2$ , there is nearly no difference at all between the data for  $X'_F = 14$ , obtained with  $T_r = 0$ , and those for  $X'_F = 22$ , obtained by applying  $T_r = 600$  K in the interval. This is because during the first period the region where the oxidizing reaction took place was entirely contained in the region where the mean temperature exceeded  $T_r$  (i.e.  $\bar{T}' \geq 1/2$  in the present case). Hence, the introduction of the temperature condition for the reaction hardly made any difference in the simulations. Indeed, figure 6 shows that only 0.1% of the oxidizer escapes without reacting. Of course, there can be no unburned carbon, since the region upstream of  $X'_F$  is constantly fed with oxidizer and remains at  $T_p > T_r$  for the present value of  $\tilde{\Delta}$ . The situation is almost the same for  $Pe_O = 5$ , with only about 1% of escaping oxidizer.



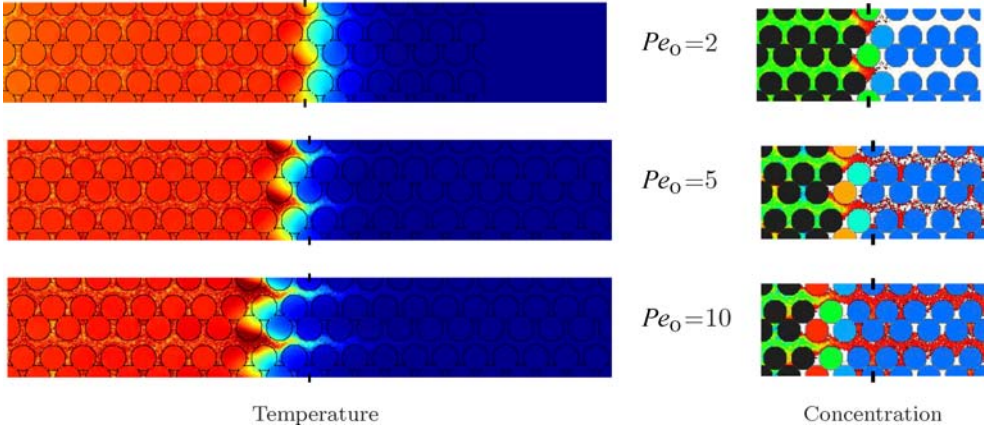


Figure 5. Temperature and concentration fields when  $X_F' = 22$  ( $Pe_O = 2$ ) or 28 ( $Pe_O = 5$  or 10), with  $\tilde{\Delta} = 0.2175$ .  $T_r$  was set to 600 K, starting from the situations shown in figure 3. The vertical marks show the position  $X_F$ .

Larger effects are observed for  $Pe_O = 10$ . In this case, about 9% of the oxygen crosses the hot region without reacting, which means that  $\Delta c_O' = 0.91$ . Hence,  $\tilde{U}_F$  in equation (14) overestimates the actual front velocity, which is given by equation (3), and indeed, the front location is found upstream of  $X_F'$  in figure 5. Moreover, the actual value of  $\Delta$  in equation (5) is larger than  $\tilde{\Delta}$  given by equation (14) and accordingly, the prediction (6) for the plateau temperature becomes  $T_p' = 1.31$  (vs. 1.28); this corresponds very accurately to the value obtained in figure 6. Because of the smaller front velocity,  $Pe_{F,s}$  also increases slightly, from 2.05 to 2.25. However, none of these changes significantly affects the physical regimes, and the same kind of intra- and inter-phase thermal disequilibrium still prevails. As a whole, the

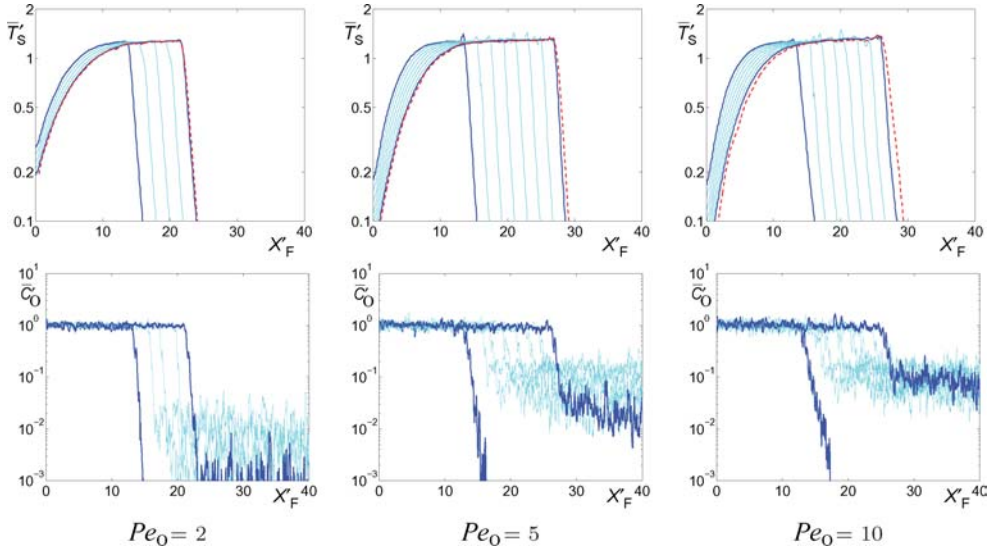


Figure 6. Profiles of the transversally averaged solid temperature  $\bar{T}_s'$  and oxygen concentration  $\bar{c}_O'$ , for  $\tilde{\Delta} = 0.2175$ .  $T_r$  is set equal to 600 K since  $X_F' = 14$ . Dark blue lines are profiles for  $X_F' = 14$  and  $X_F' = 22$  ( $Pe_O = 2$ ) or 28 ( $Pe_O = 5$  and 10). Light blue lines are for intermediate values of  $X_F'$ , by steps of 2. The red broken line is the gas temperature  $\bar{T}_g'$  in the latest stage.

only noticeable consequence of the introduction of  $T_r$  is to slow down the front propagation. Note that if  $T_r$  is set equal to 500 K instead of 600 K, it has no effect whatsoever.

### 3.2 Influence of $\tilde{\Delta}$

In this second series of calculations, the Péclet number  $Pe_O$  was kept constant and equal to 10, while the parameter  $\tilde{\Delta}$  was varied, from 0.0645 to 1.29 (see table 1). The other parameters are still given by equation (19). Different  $\tilde{\Delta}$  can be interpreted as different fuel contents in the shale (rich for large  $\tilde{\Delta}$ ) or different oxidizer concentrations in the gas (rich for small  $\tilde{\Delta}$ ). In either case, the expected front velocity and therefore  $Pe_{F,s}$  decrease as  $\tilde{\Delta}$  increases.  $Pe_{T,g}$ , which is only proportional to  $Pe_O$ , remains constant.

Results of calculations with  $T_r = 0$  are shown in figure 7 for  $X'_F = 14$ . Only the temperature fields are displayed. Since  $Pe_O$  is a constant, the reaction zones are identical in all cases, and the concentration fields all look like that in figure 3 for  $Pe_O = 10$ . However, strikingly different temperature fields result from various values of  $\tilde{\Delta}$ .

Small values of  $\tilde{\Delta}$  yield reaction-leading processes. For  $\tilde{\Delta} = 0.06$  and 0.16, the upstream hot plateau has already appeared. It is clearly visible in the transversally averaged temperature profiles in figure 8, and settles at the temperatures  $T'_p = 1.07$  and 1.19 predicted by equation (6). For  $\tilde{\Delta} = 0.32$ , the trend is obviously similar. The steady regime is not reached yet, but  $\bar{T}'_s$  and  $\bar{T}'_g$  at  $X_F$  are nearly equal to the prediction  $T'_p = 1.48$  of equation (6).

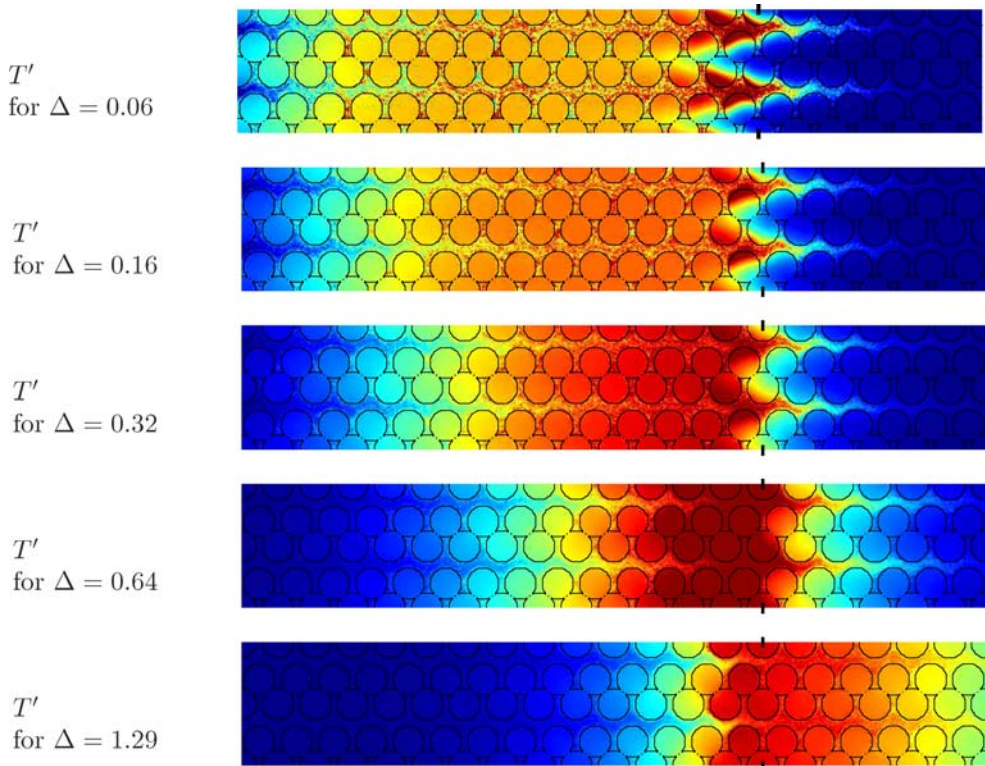


Figure 7. Temperature fields when  $X'_F = 14$ , for  $Pe_O = 10$ ,  $T_r = 0$  and various  $\tilde{\Delta}$ . The colour code is given in figure 2. The vertical marks show the position  $X_F$ .

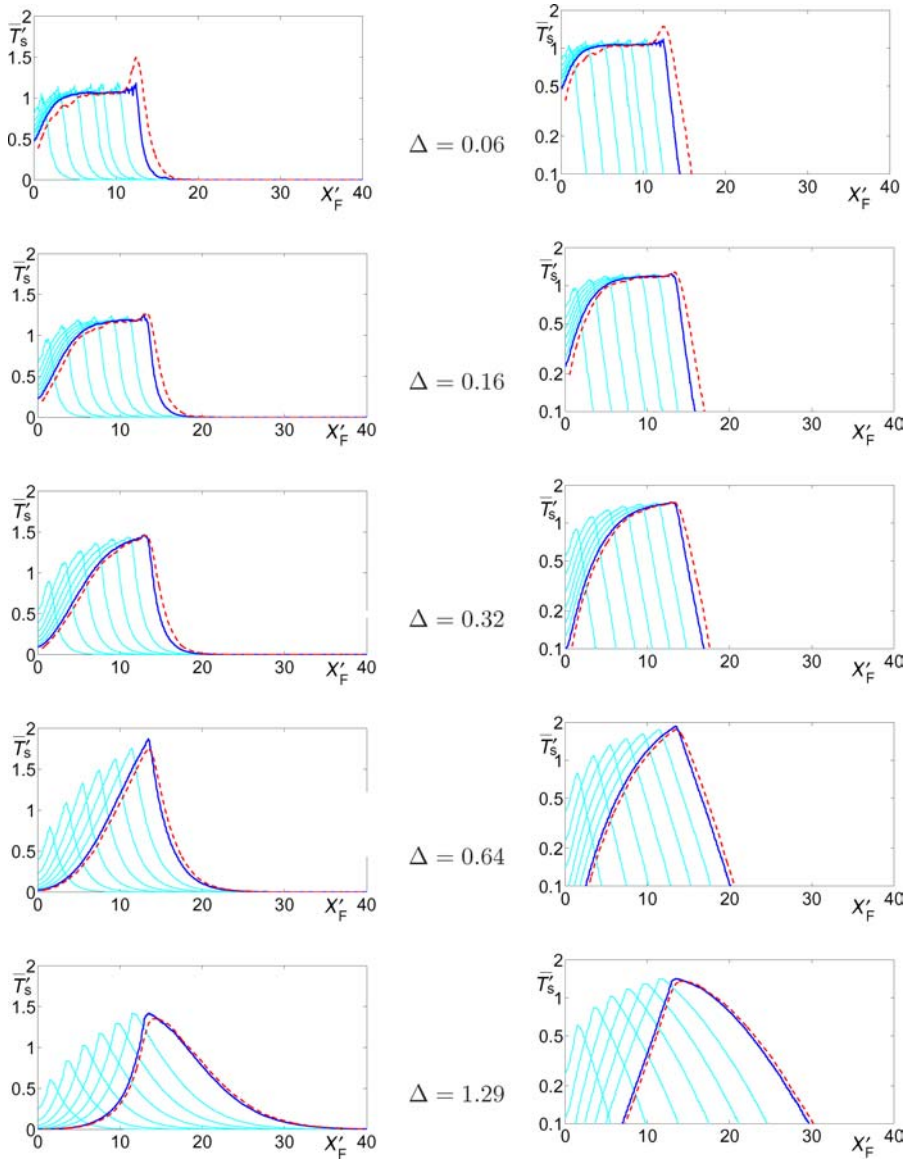


Figure 8. Profiles of the transversally averaged solid temperature  $\bar{T}'_s$ , in linear (left) and logarithmic (right) scales, for  $Pe_0 = 10$ ,  $T_r = 0$  and various  $\tilde{\Delta}$ . The profiles are given for  $X'_F = 2, 4, \dots, 12$  (light blue line) and 14 (dark blue line). The red broken line is the gas temperature  $\bar{T}'_g$  when  $X'_F = 14$ .

The two other cases with  $\tilde{\Delta} = 0.64$  and 1.29 are less clear, because they are still very far from the steady regime. The temperatures should reach  $T'_p = 2.8$  and 3.4, respectively, and they still have a lot to grow, especially in the latter case. Nevertheless, the profiles in figure 8 show without doubt that a temperature plateau is developing on the upstream side for  $\tilde{\Delta} = 0.64$  and on the downstream side for  $\tilde{\Delta} = 1.29$ , as predicted by the global arguments in Section 2.1. The plots of the temperature profiles in logarithmic scale in the right-hand column of figure 8 also make their exponential form visible, on the downstream or upstream side of the front, according to whether  $\Delta$  is smaller or larger than one (see equation (9)).

Aside from this change of global regime, there are also differences in the local thermal equilibrium status of the various cases, which result from the variations of  $Pe_{F,s}$  associated with the variations of  $\tilde{\Delta}$  (see table 1).  $Pe_{F,s}$  is smaller than unity when  $\tilde{\Delta} = 0.64$  and 1.29 and, indeed, the temperature in the solid is found to smoothly vary on the scale of the grain size. Conversely,  $Pe_{F,s}$  is larger than one for the three smaller values of  $\tilde{\Delta}$ , and especially for  $\tilde{\Delta} = 0.0645$  and 0.16. Accordingly, the solid temperature fluctuates abruptly over short distances; in the worst case with  $Pe_{F,s} \approx 7$ ,  $T'$  can vary by as much as 2 within a single solid grain.

Finally, thermal wakes in the gas show that deviations from equilibrium between the gas and solid phases exist in all cases. This is because  $Pe_{T,g} \approx 11 \gg 1$ ; when hot gas enters a cool region (or conversely), the characteristic time for diffusive transverse heat transfer is longer than the characteristic time for longitudinal convective transport.

In figure 7, local temperatures sometimes exceed the range of the colour codes defined in figure 2, i.e.  $T' > 1.5$ . This happens especially when  $\tilde{\Delta} = 0.06$  and 0.64, but for different reasons. In the latter case, it is because this region as a whole is hotter than  $1.5T_{ad}$ , and actually tends to  $T_p \approx 2.8T_{ad}$ . In the former case, the locally averaged temperature is much milder, with  $T_p \approx 1.07 T_{ad}$ , but very strong local fluctuations exist. This is clearly shown by the close-ups of the temperature maps in the reaction zone for these two cases, given in figure 9 with a modified colour code; it is actually the same colour scale applied to  $2T'$  instead of  $T'$ . It is then apparent that when  $\tilde{\Delta} = 0.06$  the solid temperature reaches locally as much as  $3T_{ad}$ , i.e. about three times the local average, whereas for  $\tilde{\Delta} = 0.64$ , the reaction front is very hot, but the variations of the temperature are very smooth.

#### 4. Matching of microscale and macroscale descriptions

In the previous section many situations have been exhibited where local thermal equilibrium is not realized, between the phases or even within each of the phases. These are *a priori* difficult to describe by use of a macroscopic model based on locally averaged state variables. However, there are cases where such an approach could be quite appropriate, and particularly those where  $Pe_{F,s}$  is smaller than one. For instance, overall local equilibrium prevails in the first case in figure 5 ( $Pe_O = 2$  and  $\tilde{\Delta} = 0.22$ ), or even in the very superadiabatic case of  $Pe_O = 10$  and  $\tilde{\Delta} = 0.64$  in figure 7.

In addition, it is likely that even though thermal equilibrium is often not satisfied near the reaction front, equilibrium is recovered at some distance from it, in quiescent regions where no heat source exists. Natural criteria in this respect are the modified Péclet numbers  $\mathcal{P}_{F,s}$  and  $\mathcal{P}_{T,g}$ , which involve the distance from the heat source:

$$\mathcal{P}_{F,s}(X) = \frac{\tilde{U}_F \mathcal{L}^2}{|X - X_F| D_{T,s}} = \frac{Pe_{F,s}}{|X' - X'_F|} \quad (20a)$$

$$\mathcal{P}_{T,g}(X) = \frac{v^* \mathcal{L}^2}{|X - X_F| D_{T,g}} = \frac{Pe_{T,g}}{|X' - X'_F|} \quad (20b)$$

They compare the characteristic times  $D_{T,s}/\mathcal{L}^2$  and  $D_{T,g}/\mathcal{L}^2$  for transverse mixing to the times  $(X - X_F)/U_F$  and  $(X - X_F)/v^*$  it takes to the front or for the gas to travel the distance  $X - X_F$ . Hence, we may expect that thermal equilibrium is recovered at the position  $X$  where  $\mathcal{P}_{F,s}$  and  $\mathcal{P}_{T,g}$  become of the order of unity. This is approximate since conduction in the solid over distances longer than  $\mathcal{L}$  depends on an effective thermal diffusivity rather than on  $D_{T,s}$ , and



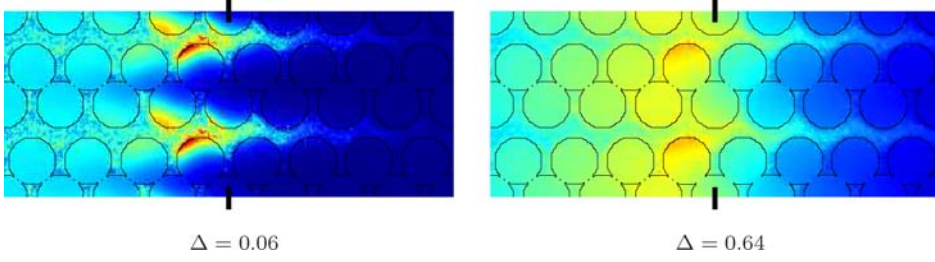


Figure 9. Close-ups of the temperature fields in the reaction zone, for  $\tilde{\Delta} = 0.06$  and  $0.64$  (see figure 7). The colour code in figure 2 is applied for  $2T'$  instead of  $T'$ . The vertical marks show the position  $X_F$ .

exchanges between the phases somewhat complicate this simple picture, but these criteria at least provide a reasonable first estimate.

This is of a great practical interest for the numerical simulations. It is indeed impossible to conduct microscale simulations on a domain covering the whole reactor, but it is not necessary either, since a coarser description is sufficient out of a relatively small active region. On the other hand, the conditions on the boundaries of the microscale simulation domain have to be

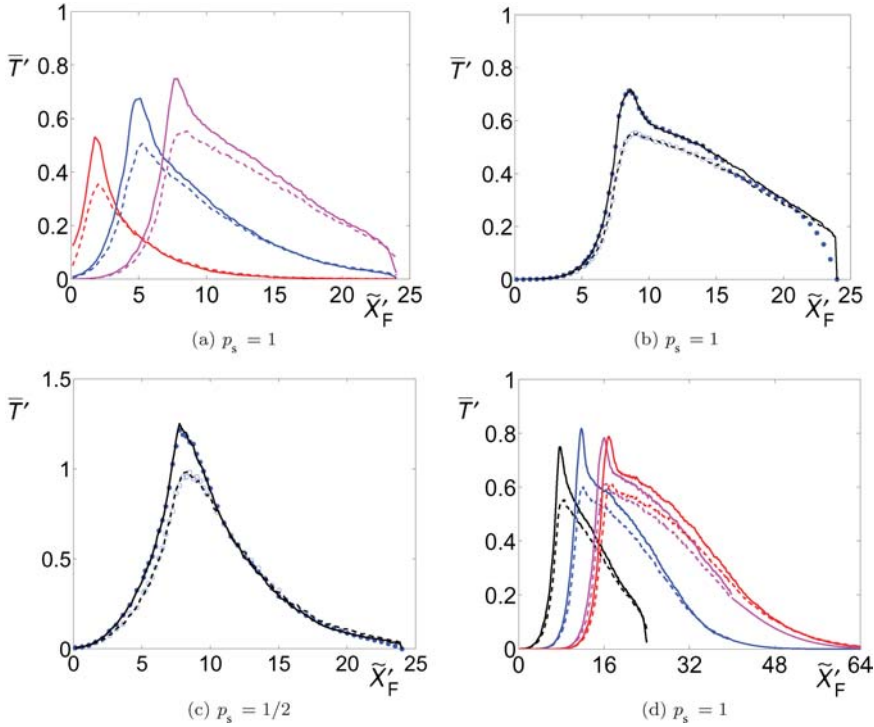


Figure 10. Profiles of the phase-averaged temperatures in a 3D random bed of grains, with  $Pe_O = 10$  and a thermal sink imposed at  $L' = 24$ . In (a), (b) and (d),  $p_s = 1$ ,  $Pe_{F,s} = 1.45$  and  $\tilde{\Delta} = 2.74$ , whereas  $p_s = 1/2$ ,  $Pe_{F,s} = 2.89$  and  $\tilde{\Delta} = 1.37$  in (c). The curves in (a) show  $\bar{T}'_s$  (—) and  $\bar{T}'_g$  (---) for successive positions  $\tilde{X}'_F = 2, 5$  and  $8$  of the reaction front. The data in (b) and (c) correspond to continuations of the calculations from  $\tilde{X}'_F = 8$  to  $\tilde{X}'_F = 9$ , with (symbols) or without (lines) matching of the microscale calculations with the macroscale model (21) at  $L'_1 = 16$ . The thermal sink in (d) is at  $L' = 800$ , and the 3D simulations are matched with equation (21) at  $L'_1 = 40$  until  $\tilde{X}'_F = 16$ , and then at  $L'_1 = 64$ . The temperature profiles are given when  $\tilde{X}'_F = 8, 12, 16$  and  $17$ . The latest stage corresponds to the 3D image of the temperature field in figure 4 of [1] (see also figure 12).

carefully set in order to prevent any spurious effects in the region of interest. A match with a macroscopic description in the far-field outer domain is a promising low-cost way to address these issues.

Let us first give an example of the kind of disturbance induced by boundary conditions which we want to eliminate. Figure 10(a) shows the profiles of the transversally average temperatures  $\bar{T}'_s$  and  $\bar{T}'_g$  when the front has reached positions  $\tilde{X}_F = 2, 5$  and  $8\Phi$  ( $\tilde{X}'_F = 2, 5$  and  $8$ ) in a 3D random bed of grains of the type of figure 3(a) of [1]. In this case,  $p_s = 1$ ,  $Pe_O = 10$  and  $Pe_{F,s} = 1.45$ . The parameter  $\tilde{\Delta} = 2.7$  is large; consequently, the downstream temperature plateau develops very fast. A thermal sink is applied at  $L = 24\Phi$ . In the early stage when  $\tilde{X}'_F = 2$ , the thermal wave has not reached yet  $L$ , and the position of this sink does not affect the processes in the vicinity of  $\tilde{X}'_F$ . In the second stage when  $\tilde{X}'_F = 5$ ,  $T$  starts increasing just upstream of  $L$ , and we can guess that the downstream boundary condition starts being felt. Finally, the disturbing influence of the downstream thermal sink is obvious when  $\tilde{X}'_F = 8$ .

Note that this happens particularly early in this simulation because of the large value of  $\tilde{\Delta}$  that we chose for this illustration. Note also that when  $\tilde{X}'_F = 5$  the mean solid and gas temperatures  $\bar{T}'_s$  and  $\bar{T}'_g$  differ significantly in the reaction zone, but thermal equilibrium between the phases is recovered at  $X'_F \approx 14$ , which is the key for the matching technique. Since the phase-averaged solid and gas temperatures eventually become very close one to another, we may expect that an upscaled single-temperature description is able to give a reasonable account of the heat transport in this quiescent region. This is subject to *a posteriori* verification, as is done in the following.

The macroscale model for this tentative description of heat transport in the far-field is a modified version of equation (8) for the transversally averaged temperature  $\hat{T}$ , where  $\hat{D}$  is replaced by  $\hat{D}^*$  which also accounts for dispersive effects

$$\frac{\partial \hat{T}}{\partial t} + \nabla \cdot [\hat{v} \hat{T} - \hat{D}^* \nabla \hat{T}] = 0 \quad (21)$$

The proper setting of the effective transport coefficients in this model is not entirely obvious, especially regarding the effective dispersive contribution. Since the first term in equation (21) represents the time derivative of the volumetric heat content,  $\hat{C}$  and  $\hat{T}$  are the volumetric averages (per transverse plane, for the latter)

$$\hat{C} = \langle C \rangle = \epsilon C_g + (1 - \epsilon) C_s \quad \hat{T} = \frac{\langle C T \rangle}{\langle C \rangle} \quad (22)$$

Since  $\bar{T}_g = \bar{T}_s = \hat{T}$ , it is natural to set the effective convective coefficient  $\hat{v}$  as

$$\hat{v} = \frac{\epsilon C_g \mathbf{v}^*}{\hat{C}} = \frac{\epsilon C_g}{\epsilon C_g + (1 - \epsilon) C_s} \mathbf{v}^* \quad (23)$$

However, the last coefficient  $\hat{D}^*$  is more difficult to figure out. It has to incorporate the conduction in the gas and solid, represented by  $\hat{D}$  in equation (8), and the dispersion by convection/diffusion in the gas, but this may not be sufficient. Indeed, the coupling of the interphase transfers with the convection introduces an additional dispersive effect. Debenest [2, section 5.6] investigated this question in detail. We only give the main result here, which is summarized in

$$\hat{D}^* = \hat{D} + \frac{\epsilon C_g}{(1 - \epsilon) C_s} D_{Tg} \tilde{D} + \frac{(\epsilon C_g)^2}{(1 - \epsilon) C_s} \frac{\mathbf{v}^{*2}}{\Gamma} \quad (24a)$$

or alternatively

$$\hat{D}^* = \hat{D} + \frac{\epsilon C_g}{(1 - \epsilon) C_s} [\tilde{D} + Pe_{T,g}^2 Da] D_{T,g}, \quad \text{with } Da = \frac{\epsilon C_g D_{T,g}}{\Gamma \mathcal{L}^2} \quad (24b)$$

Here,  $\hat{D}$  is the global effective thermal diffusivity of the porous medium,  $\tilde{D}$  results from the hydrodynamic dispersion in the gas,  $\Gamma$  is an effective interphase exchange coefficient and  $Da$  is the Damkohler number.

These coefficients can be evaluated numerically, in the medium and flow regime under consideration, by using modules of our simulation apparatus. For instance, we get  $\hat{D} = \hat{\lambda}/\hat{C} \approx 6\lambda_g/\hat{C}$  in the 3D grain beds.  $\Gamma$  and  $Da$  are obtained from the time constant of the thermal relaxation when the gas enters the porous solid at a different temperature. They are nearly independent of the flow rate.  $\tilde{D}$  is found to obey a power law of the Péclet number,  $\tilde{D} \propto Pe_{T,g}^{1.4}$ , which is a very usual behaviour [12, 13]. Consequently, the two last terms in equation (24a) can be quite important for large flow rates. The relative magnitude of the conductive term can also be small if the solid is a poor conductor; for instance, Moallemi *et al.* [14] consider wood and charcoal, with thermal conductivities three times smaller than the mineral solids in our case. In the examples in figures 10–12, the two dispersive terms are of similar magnitudes and larger than the conductive contribution.

We do not give a very detailed description of the numerical implementation of the matching technique here, because it is done in a very basic way. The 3D calculations are conducted as usual down to the abscissa  $L_1$  of the cross-over. Downstream of this position, the domain is prolonged by a virtually infinite ( $\sim 10^3 \Phi$ ) 1D continuum, where equation (21) is applied. A finite-volume time-explicit scheme is used for its simulation, with first order time discretization, centred differences for the diffusion-like term and an upwind formulation for the convective one. For convenience, the same spatial step  $a$  and time step  $\delta_t$  as in the 3D model are used. The latter is small enough by a wide margin to ensure stability. It certainly results in substantial numerical dispersion, but while the formulation is not shock-capturing, one of the main reasons why equation (21) may be applicable is that there is no shock in this region whatsoever.

Again, a thermal sink is imposed at the very far downstream boundary of the continuous medium, but it can be set at negligible cost at an arbitrary large distance  $L$ , so that it never has any influence on the simulations in the reaction zone.

As previously mentioned, the validity of the method is subject to *a posteriori* verification, and the ultimate check in this respect is the direct comparison of simulations using the matched local and macroscopic descriptions with fully 3D local simulations. Such a test is presented in figures 10 and 11. We started from the situation when the front has reached  $X_F = 8\Phi$ , with  $Pe_0 = 10$  and  $p_s = 1$ , i.e. from the final stage in figure 10(a), and from a similar case with  $p_s = 1/2$ . Both of these situations had been reached by 3D simulations with a thermal sink at  $L = 24\Phi$ . Then, the calculations were continued with exactly the same technique and parameters, until the front had progressed by an additional  $\Phi$ , and reached  $X_F = 9\Phi$ . This becomes the reference data set. On the other hand, simulations were run starting from the same situations with the part of the porous bed between  $L_1 = 16\Phi$  and the thermal sink at  $L = 24\Phi$  replaced by a continuous material, described by equation (21). This would of course be a poor choice if the purpose were to eliminate the influence of the sink, but this is not the point here. Instead, we want to try and reproduce the results of the 3D calculations under the exact same ‘physical’ conditions, which involve a sink at  $L$ . It is not even a situation where (21) can be straightforwardly expected to apply, since a significant lack of thermal equilibrium between the solid and gas exists at  $L_1$  in the initial state in the case when  $p_s = 1$ .

Nevertheless, the comparison in figure 10(b) and (c) is extremely successful. In the case of  $p_s = 1/2$ , the symbols denoting the results of the mixed micro/macroscopic model are nearly

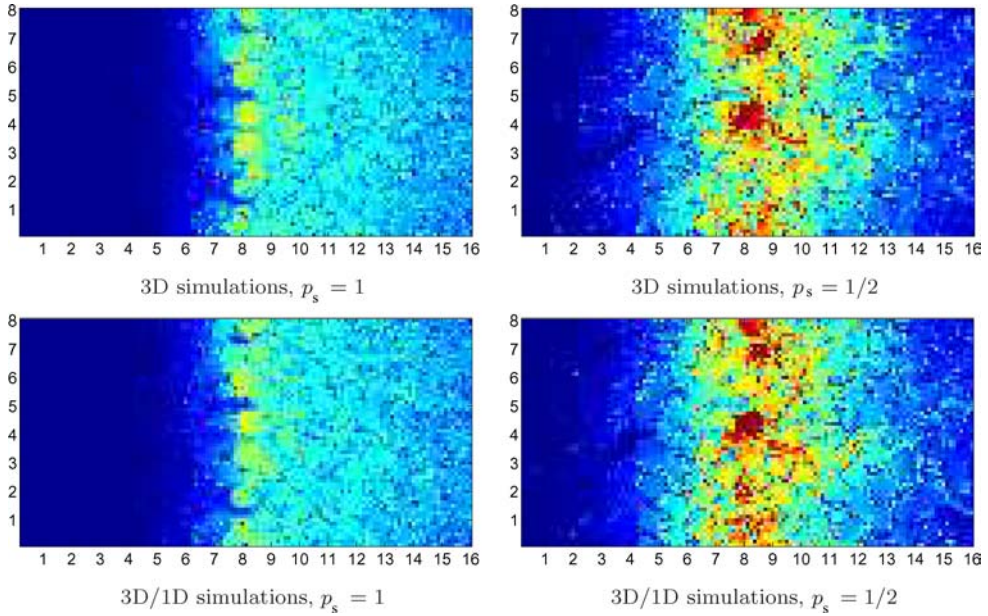


Figure 11. Temperature fields in the mid-section of the grain bed, when  $\tilde{X}'_F = 9$ , in the four cases of figures 10b,c. The colour code is given in figure 2.

superposed with the curves for the fully 3D local calculations, over the whole range  $0 \leq X'_F \leq 24$ . In the case of  $p_s = 1$ , the two separate curves for the solid and gas temperatures in the interval  $[16\Phi, 24\Phi]$  are replaced by a single value for  $\hat{T}$ , which is actually a fair approximation. But most importantly, the two simulation techniques again yield nearly identical results in the interval  $[0, 16\Phi]$ .

Furthermore, not only are the mean profiles  $\bar{T}_s$  and  $\bar{T}_g$  in good agreement, but the local temperatures are as well. Figure 11 shows the temperature fields in the mid-section of the sample, when  $X'_F = 9$ , for  $p_s = 1$  or  $1/2$ . The data obtained with or without application of the matching technique are in very good local concordance.

This test case was particularly stringent because of the large  $\tilde{\Delta}$  and flow rate. Hence, we may conclude that with reasonable precautions, a part of the porous medium where no heat is produced can be replaced by an equivalent continuum in the numerical model, without significantly affecting the results of the simulations in the rest of the domain, i.e. in the region on which the main interest is focused.

This technique was systematically applied in our 3D simulations. For instance, figure 4 of [1] shows the temperature fields in the two cases of figure 10(b) and (c), with  $p_s = 1/2$  and 1, when  $\tilde{X}'_F$  has reached 24 and 17, respectively. The profiles of  $\bar{T}'_s$  and  $\bar{T}'_g$  are shown in a few intermediate stages in figure 10(d). The thermal sink is at  $L' = 800$ . Starting from

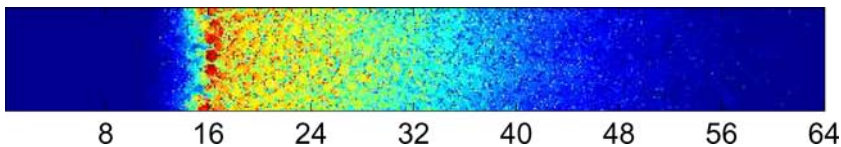


Figure 12. Temperature field in the mid-section of the random bed of grains, in the latest stage ( $\tilde{X}'_F = 17$ ) of figure 10(d). It also corresponds to figure 4 of [1]. The colour code in figure 2 is recalibrated so that the largest value corresponds to 1 instead of 1.5.

$\tilde{X}'_F = 8$ , the simulations were matched with the macroscopic model at  $L'_1 = 40$ . Because of the growing downstream temperature plateau, this had to be shifted further downstream at  $L'_1 = 64$  when  $\tilde{X}'_F$  reached 16. The temperature field in the mid-section of the bed is shown in figure 12 when  $\tilde{X}'_F = 17$ . The region where a local description is required due to a lack of mesoscale thermodynamic equilibrium is clearly visible around the reaction zone, as well as the quiescent region where the macroscopic model is applicable.

Although not actually implemented yet, it should be noted that the same matching technique which was applied on the downstream side could be used just as well upstream of the reaction zone. In the example of figures 10 and 12, and more generally in all cases where  $\tilde{\Delta} > 1$ , thermal equilibrium is fulfilled from the inlet up to a short distance from the front (see for instance the last frame in figure 7).

## 5. Conclusion

A typology of the regimes for smouldering processes in packed beds has been established. The main governing parameters have been identified from theoretical considerations in section 2, and their influence has been confirmed and illustrated by numerical simulations on the microscopic scale in section 3. Beyond the classical distinction between reaction-leading and reaction-trailing regimes, which depend on the parameter  $\tilde{\Delta}$ , simple criteria have been provided for the applicability of upscaled descriptions based on single- or double-temperature continuous models. These criteria pertain to the validity of a local thermodynamic equilibrium hypothesis, and they are based on the Péclet numbers defined in equations (15) and (17), which can be easily estimated from a limited and global knowledge.

It appears that local thermal equilibrium is not fulfilled in many cases, and especially not in the critical region where the chemical processes take place, which makes the application of macroscale models based on locally averaged state variables questionable. In such cases, a more detailed description is required in order to account for the intricate coupling of the transport and reaction mechanisms on the microscopic scale. Furthermore, even when a coarsened description is applicable, it involves several effective coefficients that are not readily accessible, since they result from the same set of coupled processes in a generally complex microstructure. Attention here was focused on the thermal transport and exchange coefficients, but similar questions are associated with the chemical species, especially the oxidizer.

Numerical simulations on the microscale are a powerful approach for both issues. Direct simulations can be conducted in severe conditions without resorting to poorly founded approximations, and effective coefficients can be determined in milder situations where they are meaningful. An example of joint application in separate domains of the same reactor of microscopic (when necessary) and macroscopic (when possible) approaches has been given in section 4.

Finally, local simulations provide a detailed knowledge of the thermochemical conditions under which the reactions occur. Thus, they can be used to study the chemical processes in more detail in order to investigate, for instance, the production of noxious species, such as CO or NO<sub>x</sub>. This will be addressed in a forthcoming paper.

## Acknowledgement

Most computations were performed at Centre Informatique National de l'Enseignement Supérieur (CINES) (subsidized by the Ministère de l'Enseignement Supérieur et de la Recherche (MESR)), whose support is gratefully acknowledged.

## References

- [1] Debenest, G., Mourzenko, V.V. and Thovert, J.-F., 2005, Smoldering in fixed beds of oil shale grains. A three-dimensional microscale numerical model. *Combustion Theory and Modelling*, **9**, 113–135.
- [2] Debenest, G., 2003, *Simulation numérique tridimensionnelle, à la microéchelle, de la combustion en lit fixe de schistes bitumineux*, PhD thesis, Poitiers.
- [3] Aldushin, A.P. and Matkowsky, B.J., 1998, Rapid filtration combustion waves driven by combustion. *Combustion Science and Technology*, **140**, 259–293.
- [4] Whale, C.W. and Matkowsky, B.J., 2001, Rapid, upward buoyant filtration combustion waves driven by convection. *Combustion and Flame*, **124**, 14–34.
- [5] Schult, D.A., Matkowsky, B.J., Volpert, V.A. and Fernandez-Pello, A.C., 1995, Propagation and extinction of forced opposed flow smolder waves. *Combustion and Flame*, **101**, 471–490.
- [6] Schult, D.A., Matkowsky, B.J., Volpert, V.A. and Fernandez-Pello, A.C., 1996, Forced forward smolder combustion. *Combustion and Flame*, **104**, 1–26.
- [7] Shkadinsky, K.G., Shkadinskaya, G.V. and Matkowsky, B.J., 1997, Filtration combustion in moving media: one and two reaction zone structures. *Combustion and Flame*, **110**, 441–461.
- [8] Aldushin, A.P., Rumanov, I.E. and Matkowsky, B.J., 1999, Maximal energy accumulation in a superadiabatic filtration combustion wave. *Combustion and Flame*, **118**, 76–90.
- [9] Aldushin, A.P. and Matkowsky, B.J., 2000, Diffusion driven combustion waves in porous media. *Combustion Science and Technology*, **156**, 221–250.
- [10] Ahd, M., Bouhafid, A., Bruel, P., Deshaies, B., Maslouhi, A., Ouhroucheand, A. and Vantelon, J.P., 2000, Report on an experimental study of smoldering in packed beds of Moroccan oil shales. Unpublished.
- [11] Nabih, K., Boukhari, A., Real, M. and Arnada, M.A.G., 1998, Physical–chemical characterization of Tarfata's oil shale R sub-zones. *Annales de Chimie-Science des Matériaux*, **23**, 389–393.
- [12] Sallés, J., Thovert, J.F., Delannay, R., Prevors, L., Auriault, J.L. and Adler, P.M., 1993, Taylor dispersion in porous media. Determination of the dispersion tensor. *Physics of Fluids A*, **5**, 2348–2376.
- [13] Coelho, D., Thovert, J.-F. and Adler, P.M., 1997, Geometrical and transport properties of random packings of spheres and aspherical particles. *Physics Review E*, **55**, 1959–1978.
- [14] Moallemi, M.K., Zhang, H. and Kumer, S., 1993, Numerical modeling of two-dimensional smoldering processes. *Combustion and Flame*, **95**, 170–182.